RESEARCH ARTICLE

SusMat WILEY

Origin of the synergistic effects of bimetallic nanoparticles coupled with a metal oxide heterostructure for accelerating catalytic performance

Wail Al Zoubi[1] | **Abdullah Al Mahmud**[2] | **Farah Hazmatulhaq**[1] | **Mohammad R. Thalji**[3] | **Stefano Leoni**[4] | **Jee-Hyun Kang**[1] | **Young Gun Ko**[1]

[1]Integrated Materials Chemistry Laboratory, School of Materials Science and Engineering, Yeungnam University, Gyeongsan, Republic of Korea

[2]School of Chemical Engineering, Yeungnam University, 280 Daehak-ro, Gyeongsan, Gyeongbuk, Republic of Korea

[3]Korea Institute of Energy Technology (KENTECH), 200 Hyeokshin-ro, Jeollanam-do, Naju, Republic of Korea

[4]Cardiff University, School of Chemistry, CF10 3AT Cardiff, United Kingdom

Correspondence
Wail Al Zoubi and Young Gun Ko, Integrated Materials Chemistry Laboratory, School of Materials Science and Engineering, Yeungnam University, Gyeongsan 38541, Republic of Korea.
Email: wailalzoubi@ynu.ac.kr and younggun@ynu.ac.kr

Abstract

Precisely tuning bicomponent intimacy during reactions by traditional methods remains a formidable challenge in the fabrication of highly active and stable catalysts because of the difficulty in constructing well-defined catalytic systems and the occurrence of agglomeration during assembly. To overcome these limitations, a PtRuPNiO@TiO$_x$ catalyst on a Ti plate was prepared by ultrasound-assisted low-voltage plasma electrolysis. This method involves the oxidation of pure Ti metal and co-reduction of strong metals at 3000°C, followed by sonochemical ultrasonication under ambient conditions in an aqueous solution. The intimacy of the bimetals in PtRuPNiO@TiO$_x$ is tuned, and the metal nanoparticles are uniformly distributed on the porous titania coating via strong metal–support interactions by leveraging the instantaneous high-energy input from the plasma discharge and ultrasonic irradiation. The intimacy of PtRuPNiO@TiO$_x$ increases the electron density on the Pt surface. Consequently, the paired sites exhibit a high hydrogen evolution reaction activity (an overpotential of 220 mV at a current density of 10 mA cm^{-2} and Tafel slope of 186 mV dec^{-1}), excellent activity in the hydrogenation of 4-nitrophenol with a robust stability for up to 20 cycles, and the ability to contrast stated catalysts without ultrasonication and plasma electrolysis. This study facilitates industrially important reactions through synergistic chemical interactions.

KEYWORDS
bimetals, nanoparticles, oxides, heterostructures, hydrogenation

1 | INTRODUCTION

Research on bimetallic catalysts has substantially increased over the past few decades owing to their unique catalytic and electronic properties compared with their single-metal counterparts. These properties arise from the direct contact between the different metals, which can be exploited to achieve synergistic effects.[1,2] However, the synergistic effects, namely, short- or long-range interactions, of bimetallic catalysts are poorly understood. Furthermore, the active sites of these catalysts are unidentified, and their sizes cannot be reduced to below 10 nm because high temperatures expedite atomic-scale diffusion and particle growth.[3] This is due to the restrictions on controlling the catalyst microstructure and accurately tuning the intimacy of bimetals via basic methods, such as thermal decomposition of metallic precursors, electrochemical synthesis, chemical reduction, radiolysis, and sonochemical synthesis.

Bifunctional catalysis can be achieved by enhancing the constructed interfaces and electronic interactions between bimetallic atoms through short-range forces. In such cases, the electronic interactions between the metal atom and metal oxide promoter lead to the formation of multiple potential active sites in the bifunctional catalyst under reduction reaction conditions. Current studies have demonstrated the intimacy effects (proximity) of dissimilar catalyst components on the catalytic performance when the components are isolated as single nanoparticles (NPs) and interact via long-range forces at millimeter-scale distances.[4–11] For example, Phaahlamohlaka et al. reported the effects of intimacy on hydrogen spillover using Fischer–Tropsch catalysts supported on mesoporous hollow carbon spheres (MHCSs). The catalysts were prepared by conventional wet impregnation, in which Ru was loaded inside and outside the MHCSs, whereas Co_3O_4 and NiO were loaded on the outer layer of the MHCSs.[6] Karim et al. reported the accurately controlled intimacy in Pt–FeO_x catalysts at nanoscale distances. The components were encapsulated in the macropores of a hierarchically structured SiO_2 support using an accurate nanolithography method, and effects of the TiO_2 and Al_2O_3 supports on hydrogen spillover were examined.[8] Although metal-oxide-supported catalysts exhibiting intimacy effects at the atomic scale have been successfully fabricated, this process typically involves complex synthesis methods, strenuous post-modifications, or the use of expensive or sophisticated equipment.[7–9] Overall, conventional methods for synthesizing bicomponent catalytic systems currently face challenges such as restrictions on controlling the catalyst microstructure and accurately tuning the intimacy of the bimetals. Therefore, a simpler synthesis method for metal-oxide-supported bicomponent catalysts that enables

rational tuning of intimacy is urgently needed. Furthermore, a better understanding of the chemical structures, catalytic performance, and catalytic mechanism of these catalysts is required to accelerate the development and application of these bicomponent systems in heterogenous catalysis.

To this end, we studied the intimacy effects of TiO_2-supported ultrasmall (us)-PtMPNiNiO (M = Ru, Ga, In) catalysts on hydrogen spillover and the selective hydrogenation of 4-nitrophenol (4-NP). The PtMPNiNiO@TiO_2 catalysts were prepared using a highly controllable and dependable ultrasound-assisted low-voltage plasma electrolysis (LV-PE) approach under ultrasonic irradiation. LV-PE is a powerful strategy that has been used in recent decades to synthesize sophisticated conformal porous supports.[11,12] Compared with PtInPNiNiO@TiO_2 and PtGaPNiNiO@TiO_2, PtRuPNiNiO@TiO_2 exhibited outstanding catalytic performance and selectivity in 4-NP hydrogenation (Scheme 1). The fabricated PtRuNiNiO@TiO_2 catalyst also displayed enhanced hydrogen evolution reaction (HER) activity with a significantly decreased overpotential of 220 mV at 10 mA cm^{-2} in 0.5 M H_2SO_4. It significantly outperformed other reported catalysts; for instance, its mass activity was 20.6 A mg^{-1} at an overpotential of 100 mV, which is 41 times higher than that of a commercial NiNiO@TiO_2 catalyst. The LV-PE protocol can be easily extended to various bifunctional catalysts with bimetallic components to achieve synergistic effects and improved activities in reduction reactions.

2 | RESULTS AND DISCUSSION

2.1 | Synthesis and characterization of PtM-PNiNiO@TiO_x

The application of the PtM-PNiNiO/TiO_x catalyst on a pure Ti plate is shown in Scheme 1. Briefly, PtM-PNiNiO@TiO_x was synthesized using a one-pot ultrasound-assisted coincident electro-oxidation–reduction–precipitation (U-SEO-P) method. This method involves simultaneous co-reduction of mixed metal salts and oxidation of the Ti substrate to form single-phase PtMPNi NPs deposited on the TiO_2 support for enhanced catalysis. PtM–PNiNiO NPs were chosen to exert maximum control over multielement NP dispersion by sonochemical ultrasonication. A high loading amount of the NPs (8 wt%) was used to produce a brown porous coating on the surface of the gray Ti substrate at plasma discharge temperatures between 2000°C and 3000°C. The measured loading capacity of the TiO_x support was
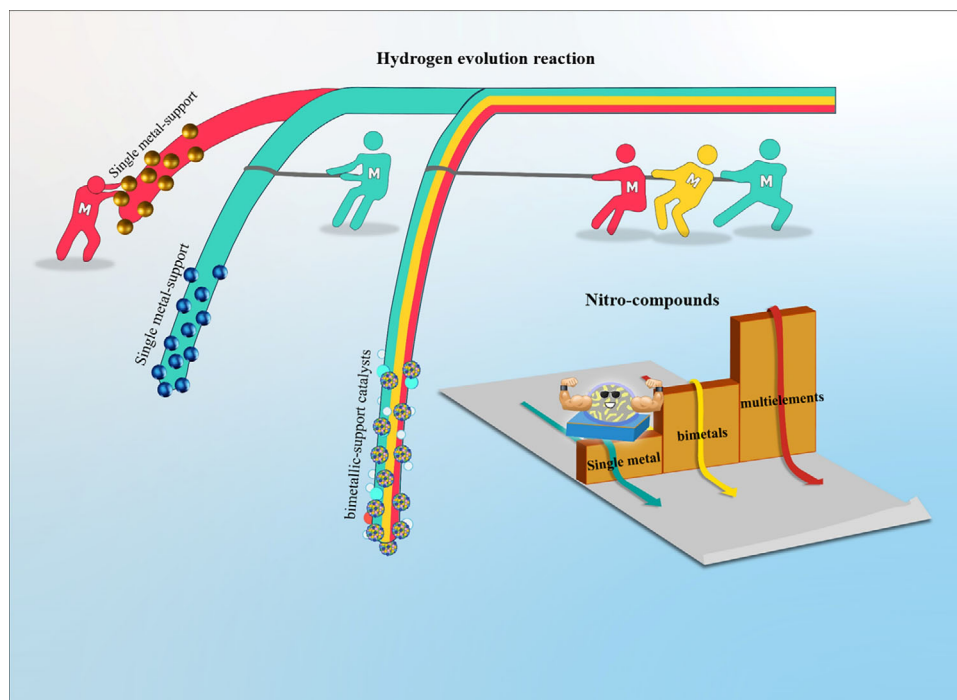
S C H E M E 1 Schematic of the catalytic performance of bimetallic support catalysts prepared via ultrasound-assisted coincident electro-oxidation–reduction–precipitation process.

approximately 3.02 mg cm^{-2}.[13] Sonochemical ultrasonication was performed in an aqueous solution under ambient conditions to achieve the uniform dispersion and co-reduction of the metal salts of the catalysts with dissimilar loadings.

Powder X-ray diffraction (PXRD) analysis provided evidence of the effective synthesis of the PtM-PNiNiO@TiO$_x$ catalysts and showed that the PtM-PNiNiO NPs had a face-centered cubic structure (Figure S1). This result was further confirmed by the high-angle annular dark-field scanning transmission electron microscopy (HAADF-STEM) images shown in Figure 1. The us-PtM-PNiNiO NPs were uniformly dispersed on the porous TiO$_x$ supports with an average size of approximately 2 nm (Figure 1A–I), which is smaller than those of other metal oxide NPs.[11–15] The lack of clear peaks in the PXRD patterns of the PtM-PNoNiO NPs (Figure S1) confirmed the formation of us-crystals. These results agree with previous research on small metal nanocrystals[14] and the HAADF-STEM and energy-dispersive X-ray spectroscopy (EDS) results for the single us-PRu-PNiNiO NP (Figure 1J–I). Thus, PtM–PNiNiO NPs were uniformly deposited on the outer layer of the TiO$_x$ support and well-mixed without compositional aggregation, indicating the effectiveness of our U-SEO-P strategy for preparing a strong TiO$_x$ support for PtM–PNiNiO NPs. To confirm the strong interactions between the support and NPs, heat treatment was performed at 600°C. No significant changes in the size of the PtM–PNiNiO NPs were

observed (Figure S2). HAADF-STEM and high-resolution transmission electron microscopy (HRTEM) images of PtRu-PNiNiO@TiO$_x$ with the corresponding fast Fourier transform images clearly showed that the us-PtM-PNiNiO NPs were uniformly encapsulated in the amorphous-like porous TiO$_x$ support (Figure 1D–I,M,N). NiO NPs with a small size of approximately 18 nm and low melting point of approximately 1955°C can be easily incorporated into a TiO$_x$ support if they have relatively high chemical stability, resulting in a higher fraction of the amorphous phase in the layer.[15] The lattice spacing along the [011]-zone axis was 0.218 nm, suggesting that the us-PtM-PNiNiO NPs had a (111) base plane. The lattice spacing of 0.360 nm corresponded well with the (101) plane of anatase TiO$_x$. The Pt/Ru/P/Ni atomic ratio was 0.48:0.20:0.23:0.07 (Figure 1I), which qualitatively agrees with the results of previous inductively coupled plasma-atomic emission spectroscopy (ICP-AES) analyses.[12] Long-term exposure to electron beams during elemental mapping severely damages NPs. Therefore, larger NPs were chosen to obtain clear elemental mappings.

Furthermore, the chemical states of the metals were determined by X-ray photoelectron spectroscopy (XPS). Figure 2A shows the double peaks of Ti 2p at 458.12 and 463.92 eV corresponding to Ti 2p$_{3/2}$ and Ti 2p$_{1/2}$, respectively, which confirms the fabrication of NiO-doped TiO$_x$.[16] The appearance of the Ti^{3+} peak at 458.4 eV indicates that oxygen was eliminated from the lattice after
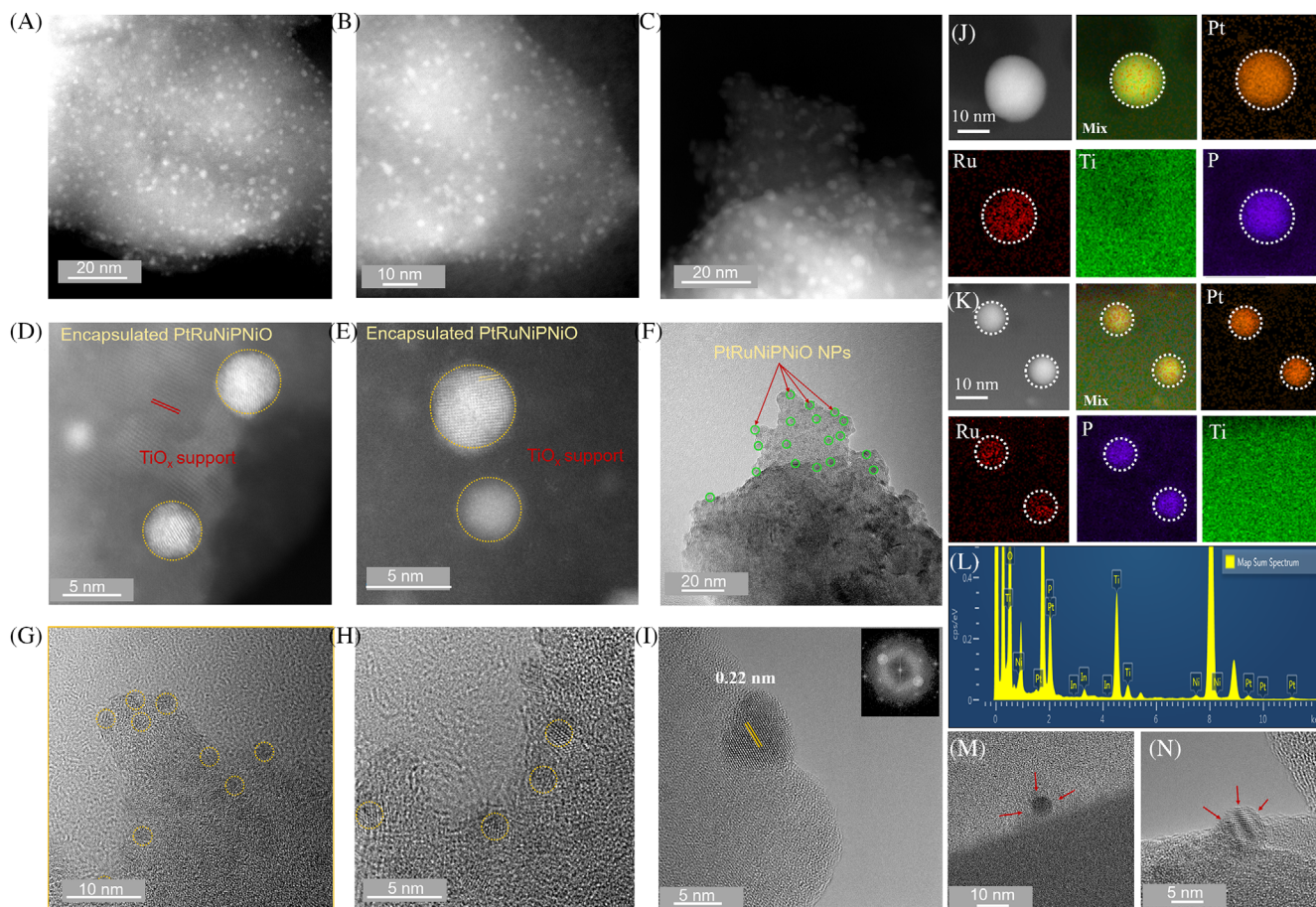
FIGURE 1 Structural characterization of us-PtM-PNiNiO@TiO$_x$ catalysts. High-angle annular dark-field scanning transmission electron microscopy (HAADF-STEM) images of (A) us-PtGaPNiNiO@TiO$_x$, (B) us-PtInPNiNiO@TiO$_x$, and (C) us-PtRuPNiNiO@TiO$_x$. (D and E) HAADF-STEM images and lattice spacing of the single PtRuPNi indicated in (c). (F–I) Low-magnification high-resolution transmission electron microscopy (HRTEM) images of us-PtRuPNiNiO@TiO$_x$. (J and K) HAADF-STEM image of a single us-NP and the corresponding energy-dispersive X-ray spectroscopy (EDS) elemental mappings of Pt, Ru, P, and Ti. (M and N) HRTEM image of encapsulated PtRuPNi NPs in us-PtRuPNiNiO@TiO$_x$. The red arrows indicate the overlayer.

the U-SEO-P reactions. The shift in the Ti 2p peaks to higher binding energies (BEs) in the XPS spectrum of us-PtRu-PNiNiO@TiO$_x$ suggests a low electron density at the NiO@TiO$_x$ surface in the presence of us-PtRuPNi-NPs, which confirms the strong interactions between them. The low electron density is due to the reaction of Ti^{4+} with electrons from either the ultrasonic irradiation and plasma discharge treatment itself or the oxygen vacancies it generates on the support surface. To confirm the presence of oxygen vacancies, Mott–Schottky plots of the TiO$_x$ support were obtained (Figure S3). The positive slopes of the linear parts of the plots indicate the n-type semiconducting properties of the grown TiO$_x$ due to electron donation by oxygen vacancies and metal interstitials in the support structure. Above −0.5 V, the plots became non-linear because of an increase in the depth of the region depleted of donor density.[17] The Ni 2p XPS spectra of the us-PtRuPNiNiO@TiO$_x$, us-PtRuPNiNiO@TiO$_x$,

and us-PtRuPNiO@TiO$_x$ catalysts showed two spin-orbit doublets (Figure 2B). The Ni 2p$_{3/2}$ main peak at approximately 855.38 eV and its shake-up satellite at approximately 860.37 eV and the Ni 2p$_{1/2}$ main peak at approximately 873.34 eV and its shake-up satellite at approximately 878.92 eV confirmed the existence of NiO.[18] Interestingly, the Ru 3p XPS spectrum of us-PtRuPNiO@TiO$_x$ showed only the metallic peaks of Ru 3p$_{1/2}$ and Ru 3p$_{3/2}$ at 457.85 and 463.61 eV, respectively, without any of the oxidized peaks exhibited by PtRuP-based catalysts (Figure 2E). The Ga (3d) core-level spectrum of us-PtGaPNiNiO@TiO$_x$ showed two chemical states, namely Ga(0) (16.26 eV) and Ga(III) (23.02 eV), which confirmed the existence of us-PtGaP-NPs on the surface of the NiO@TiO$_x$ support (Figure 2F). In the In 3d XPS spectra, the peaks near 452.11 and 443.85 eV corresponding to In 3d$_{3/2}$ and In 3d$_{5/2}$, respectively, were assigned to In^{3+}, whereas those at 451.48 and 444.73 eV were assigned to In^0 NPs, in
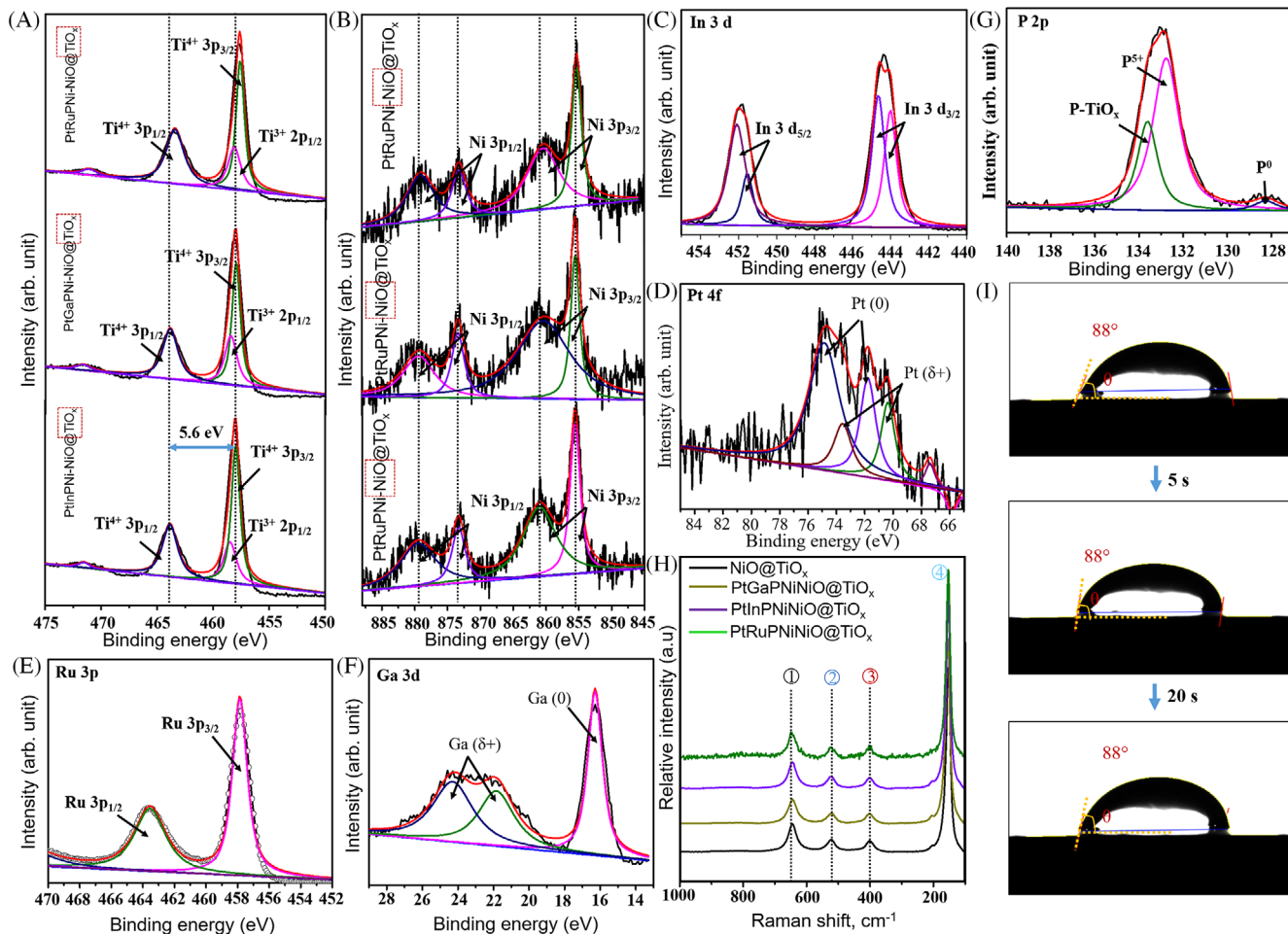
FIGURE 2 X-ray photoelectron spectra of (A) Ti 2p, (B) Ni 3p, (C) In 3d, (D) Pt 4f, (E) Ru 3p, (F) Ga 3p, and (G) P 2p. (H) Raman results of the NiO@TiO$_x$, us-PtGaPNiNiO@TiO$_x$, us-PtInPNiNiO@TiO$_x$, and us-PtRuPNiNiO@TiO$_x$ catalysts. (I) The contact angle of us-PtGaPNiNiO@TiO$_x$ using water as the solvent.

accordance with previous literature (Figure 2C).[19] The Pt 4f XPS spectrum of us-PtRuPNiO@TiO$_x$ was deconvoluted into pairs of doublets. The two peaks at 74.84 and 71.77 eV were attributed to Pt^0 4f$_{5/2}$ and Pt^0 4f$_{7/2}$, respectively, and a small fraction of Pt existed as Pt^{II} (Figure 2D).[20] The peaks in the Pt 4f XPS spectra of us-PtGaPNiNiO@TiO$_x$ and us-PtInPNiNiO@TiO$_x$ shifted to higher BEs relative to those of us-PtRuPNiNiO@TiO$_x$. This shift (>0.36 eV) indicates the strong electronic interactions between Pt and the us-NPs on its surface (Figures S3 and S4). In addition, the peaks at 128.98 and 133.4 eV in the P 2p XPS spectra were attributed to elemental P^0 and oxidized P, respectively, whereas the peak at 132.6 eV corresponded to P^{5+} (Figure 2G).[21] These results imply strong metallic interactions between Pt, Ru, and P on the NiO@TiO$_x$ surface, which can be attributed to the formation of a Pt–Ru–P alloy. The four bands at 647 cm^{-1} (E$_g$), 517 cm^{-1} (B$_{1g}$), 400 cm^{-1} (B$_{1g}$), and 150 cm^{-1} (E$_g$) in the Raman spectra of the catalysts confirmed the existence of NiO−TiO$_x$ (Figure 2H). Encouraged by these results, the wetting properties of the

Pt–P–Ru@NiOTiO$_2$ system, which was used as a multielement NP–support system, were measured by determining the water contact angle. As shown in Figure 2I, the droplets were stable for a considerably longer time when the surface was coated with PtRuP@NiOTiO$_2$ under ultrasonic irradiation. The shape of the water droplets and contact angle of approximately 83° at room temperature remained constant during a long period of 20 s. These results clearly demonstrate the stability of the surface properties of NPs supported on Ni and Ti oxides.

2.2 | Catalytic performance of us-PtM-NiO@TiO$_2$

The reduction of 4-NP to 4-aminophenol (4-AP) was conducted in the presence of us-PtRuPNiO@TiO$_x$, us-PtInPNiNiO@TiO$_x$, us-PtGaPNiNiO@TiO$_x$, and us-PtNiNiO@TiO$_x$ catalysts. The best catalytic performance was achieved using us-PtRuPNiO@TiO$_x$ in an aqueous
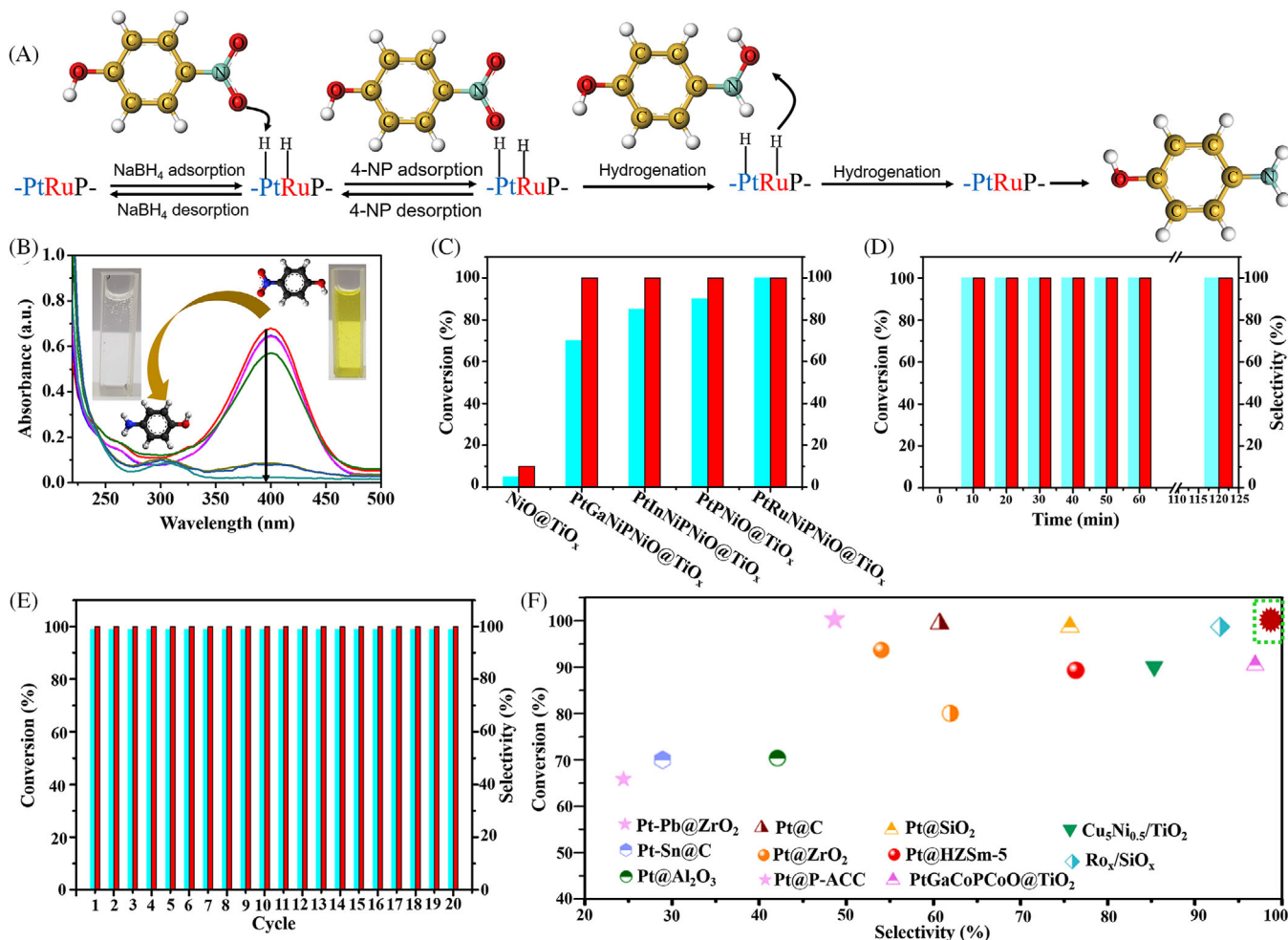
FIGURE 3 (A) Proposed reaction pathway of the reduction of 4-nitrophenol (4-NP) to 4-aminophenol (4-AP) on the us-PtRuPNiNiO@TiO$_x$ surface. (B) Ultraviolet (UV)–visible diffuse reflectance spectra of 4-NP in a NaBH$_4$ solution with the us-PtRuPNiNiO@TiO$_x$ catalyst. (C) Catalytic activities of the us-NiO@TiO$_x$, us-PtGaPNiNiO@TiO$_x$, us-PtInPNiNiO@TiO$_x$, us-PtPNiNiO@TiO$_x$, and us-PtRuPNiO@TiO$_x$ catalysts under the same conditions. (D) Catalytic performance of us-PtRuPNiNiO@TiO$_x$ during 125 min of reaction. (E) Recyclability of us-PtRuPNiNiO@TiO$_x$ for the hydrogenation of 4-NP to 4-AP. (F) Comparison of the catalytic performances of us-PtRuPNiNiO@TiO$_x$ and recently reported Pt-based catalysts in terms of conversion and selectivity.

solution at room temperature (Figure 3A–C). This may be due to the formation of more Ru aggregates that produce nanoclusters, which decreased the activation ability of the catalyst. The us-PtRuP NPs in the NiO@TiO$_x$ support accelerated electron transfer from NaBH$_4$, which was used as the reducing agent, to the electron acceptor, 4-NP which was consequently reduced to 4-AP (Figure 3A). Moreover, the reduction of 4-NP was enhanced by us-PtRuPNiNiO@TiO$_x$ because the PtRu sites acted as a coordination environment for hydrogenation activity.[22] It has been proposed that hydrogenation proceeds via a direct pathway: HO-Ar-NO$_2$ → HO-Ar-NOOH → HO-Ar-N(OH)$_2$ → HO-Ar-NH$_2$. However, other studies have suggested an indirect hydrogen-assisted pathway, which begins with HO-Ar-NO$_2$ adsorption and ends with the attack of H* spilled from the PtRu sites because of the low-
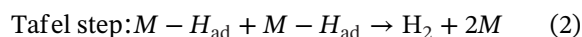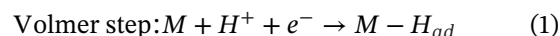
ered energy barrier for N–O bond breaking: HO-Ar-NO$_2$ → HO-Ar-NOOH* → HO-Ar-N(OH)$_2$ → HO-Ar-NOH → HO-Ar-NHOH → HO-Ar-NH → HO-Ar-NH$_2$. For the us-PtRuPNiO@TiO$_x$ catalyst, the energy barrier for the direct pathway (~4 eV) was higher than that for the indirect pathway (1.76 eV), demonstrating that the indirect pathway is more plausible.[23,24] The detailed pathways are shown in Figure 3B,C. It is well known that color of the 4-NP solution changes from light yellow to bright yellow after the addition of a reducing agent owing to the formation of 4-nitrophenolate. The absorption peak at 400 nm in the ultraviolet–visible diffuse reflectance spectrum did not change within 30 min without the addition of a catalyst to the mixture (Figure 3B), suggesting that the reducing agent alone could not reduce 4-NP. After the addition of us-PtRuPNiNiO@TiO$_x$, the intensity of the absorption

peak at 400 nm decreased rapidly. The mixture became colorless when the catalytic reduction was complete. When the amount of us-PtRuPNiNiO@TiO$_x$ was only 4 mg, the peak at 400 nm vanished within 60 s. The catalytic performance in the reduction of p-nitrobenzene (as a model substrate) to p-aminophenol was examined under mild conditions using NaBH$_4$ as the reducing agent. No reduction reaction was observed using either TiO$_2$ or NiO–TiO$_2$ (Table S1). In contrast, an extraordinarily high conversion (100%) within 1 min and high selectivity (100%) toward p-aminophenol were observed using us-PtRuPNiNiO@TiO$_x$ (Figure 3B). Furthermore, the conversion and selectivity remained constant when the reduction time was extended to 2 h (Figure 3D), indicating the high activity of us-PtRuPNiO@TiO$_x$. ICP-AES analysis confirmed that no NPs were leached during the reaction. The use of us-PtGaPNiNiO@TiO$_x$ and us-PtInPNiNiO@TiO$_x$ also yielded p-aminophenol albeit with a slow 4-NP conversion. Remarkably, us-PtRuPNiNiO@TiO$_x$ exhibited outstanding recycling stability (nearly 100% after 20 successive rounds) in terms of both conversion and selectivity (Figure 3E). After recycling, no noticeable structural changes in us-PtRuPNiNiO@TiO$_x$ were observed (Figures S5 and S6), and Pt or In leaching to the reaction solution did not occur. Only 0.030 wt% of PtRuP was detached from the fresh us-PtRuPNiNiO@TiO$_x$ catalyst, indicating that NiO@TiO$_x$ can stabilize us-PtRuP against leaching. These results confirm the strong electronic interactions between PtRuP and the NiO@TiO$_x$ support. A comparison of the conversion and selectivity of dissimilar catalysts (Figure 3F) showed that us-PtRuPNiNiO@TiO$_x$ has the highest catalytic efficiency among the reported Pt-based catalysts.[22–27]

2.3 | Electrochemical performance of us-NPs

The HER activities of us-PtRuPNiNiO@TiO$_x$, us-PtGaPNiNiO@TiO$_x$, us-PtInPNiNiO@TiO$_x$, us-PtPNiNiO@TiO$_x$, and NiNiO@TiO$_2$ were evaluated using a standard three-electrode setup in 0.5 M H$_2$SO$_4$ electrolytes at room temperature and a current density of 10 mA cm^{-2} (Figure 4A–F). The overpotential of these catalysts were 224, 442, 371, 291, and 595 mV, respectively (Figure 4A). In addition, us-PtRuPNiO@TiO$_x$ had a Tafel slope of 186 mV dec^{-1}, which was smaller than those of us-PtGaPNiO@TiO$_x$ (234 mV dec^{-1}), us-PtInPNiO@TiO$_x$ (212 mV dec^{-1}), us-PtPNiO@TiO$_x$ (201 mV dec^{-1}), and NiO@TiO$_x$ (305 mV dec^{-1}) (Figure 4B). The Ru$_{0.5}$Pt$_{0.5}$NiO@TiOx catalyst exhibited the best HER activity compared with Ru$_{0.5}$NiO@TiO$_x$, Pt$_{0.5}$NiO@TiO$_x$,

and Ru$_{0.3}$Pt$_{0.7}$NiO@TiO$_x$ (Figure S8). It should be noted that the overpotential of Ru$_{0.5}$Pt$_{0.5}$NiO@TiO$_x$ at 10 mA cm^{-2} was 224 mV, which is approximately 4.3, 3.0, and 2.5 times those of Ru$_{0.5}$NiO@TiO$_x$, Pt$_{0.5}$NiO@TiO$_x$, and Ru$_{0.3}$Pt$_{0.7}$NiO@TiO$_x$, respectively. Additionally, the Tafel slopes of Ru$_{0.5}$NiO@TiO$_x$, Pt$_{0.5}$NiO@TiO$_x$, and Ru$_{0.3}$Pt$_{0.7}$NiO@TiO$_x$ were 350, 308, and 291 mV dec^{-1}, respectively (Figure S9). These results prove the importance of the synergistic effects of Ru and Pt in the Ru$_{0.5}$Pt$_{0.5}$NiO@TiO$_x$ catalyst, which enhance electron transfer and conductivity inside the bimetal NPs. Interestingly, the electrocatalytic performance was reduced when the Pt content was increased. This indicates that a high Pt content in the catalyst can block the formation of active sites, which play a vital role in electrocatalytic reactions, thereby negatively affecting the catalytic performance.[28,29] The Tafel slope suggests that the reaction mechanism follows the four steps described by Volmer and Tafel.[29]

$$\text{Volmer step:} M + H^+ + e^- \rightarrow M - H_{ad} \qquad (1)$$

$$\text{Tafel step:} M - H_{ad} + M - H_{ad} \rightarrow H_2 + 2M \qquad (2)$$

where M denotes the number of active sites in the catalyst and H_{ad} is the active site of the catalyst. First, a H$^+$ ion attaches to H_{ad}. Subsequently, two adsorbed H_{ad} species produce one H$_2$ molecule. Therefore, adsorption on the active site is the rate-determining step of this type of reaction. The double-layer capacitance (C_{dl}) is proportional to the number of electrochemically active sites. This was determined by conducting cyclic voltammetry across a voltage range of 0.05–0.15 V (vs. reversible hydrogen electrode) at various scan rates (Figure S7). ΔJ, which is the difference between the anodic and cathodic current densities, was then plotted against the scan rate to obtain C_{dl}.[30–34] The corresponding double-layer cyclic voltammograms are shown in Figure 4C. The C_{dl} values were 0.14, 0.20, 0.28, 0.32, and 0.39 mF cm^{-2} for NiO@TiO$_x$, us-PtGaPNiO@TiO$_x$, us-PtInPNiO@TiO$_x$, us-PtPNiO@TiO$_x$, and us-PtRuPNiO@TiO$_x$, respectively. This indicates that us-PtRuPNiO@TiO$_x$ had the highest number of catalytically active sites. Thus, it can facilitate faster H$^+$ diffusion to the active sites for the catalytic reaction. In addition, the electrochemical surface area (ECSA) is an important parameter of electrocatalysts that is widely used to assess the number of active sites, which directly correlates with the density of the electroactive sites participating in the reaction.[32,33]

The ECSA is calculated using the following equation[35]:

$$ECSA = \frac{C_{dl}}{C_s} = \frac{C_{dl}}{0.04(\text{mF cm}^{-2})\text{ per cm}^2} \qquad (3)$$
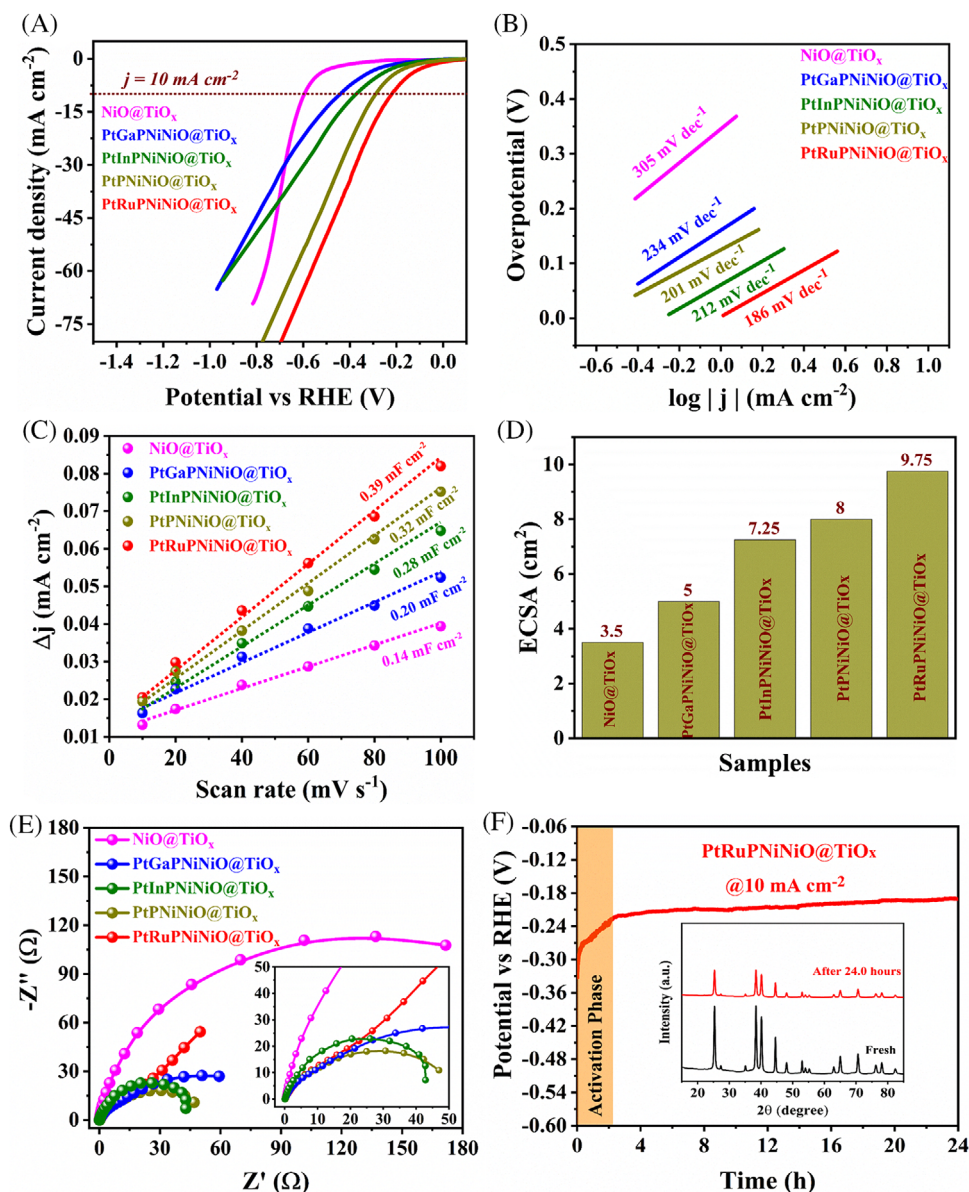
FIGURE 4 Experimental results for the hydrogen evolution reaction (HER) of the electrocatalysts in 0.5 M H_2SO_4. (A) Linear sweep voltammetry curves, (B) Tafel plots, (C) double-layer capacitance (C_{dl}) values, (D) electrochemical surface areas (ECSAs), (E) Nyquist plots, and (F) cyclic voltammetry curves in the double-layer regions.

where C_s is the specific capacitance, which is 0.04 mF cm^{-2} for a flat surface.[6]

The ECSA values of us-PtRuPNiO@TiO$_x$, us-PtGaPNiNiO@TiO$_x$, us-PtInPNiNiO@TiO$_x$, us-PtPNiNiO@TiO$_x$, and NiNiO@TiO$_x$ were 9.75, 5, 7.52, 8, and 3.5 mF cm^{-2}, respectively (Figure 4D). The higher ECSA of us-PtRuPNiNiO@TiO$_x$ resulted from the preferential formation of Pt over Ru, the large number of active sites on the surface, and the synergistic effects of numerous factors, such as the high alloying degree, considerable accessible active sites, high miscibility, and strong electronic interaction between Ru and Pt atoms.[30] Electrochemical impedance spectroscopy was performed

for all the catalysts to obtain the Nyquist plots (Figures 4E and S8). us-PtRuPNiO@TiO$_x$ had a smaller charge transfer resistance than the other catalysts. This indicates the first charge transfer during the electrocatalytic HER. In addition, Figure 4F shows the chronopotentiometric stability analysis for us-PtRuPNiNiO@TiO$_x$ at 10 mA cm^{-2}. The catalyst exhibited excellent stability for 16 h, where the first 1.5 h was the activation phase for reaching a fixed potential. To confirm our results, the impact of composition and disorder on the electronic structure of PtRuPNiO was investigated with density functional theory calculations. From NiO to PtRuPNiO over RuNiO and PtRuNiO, the evolution of the projected density of states (PDOS) (*d*
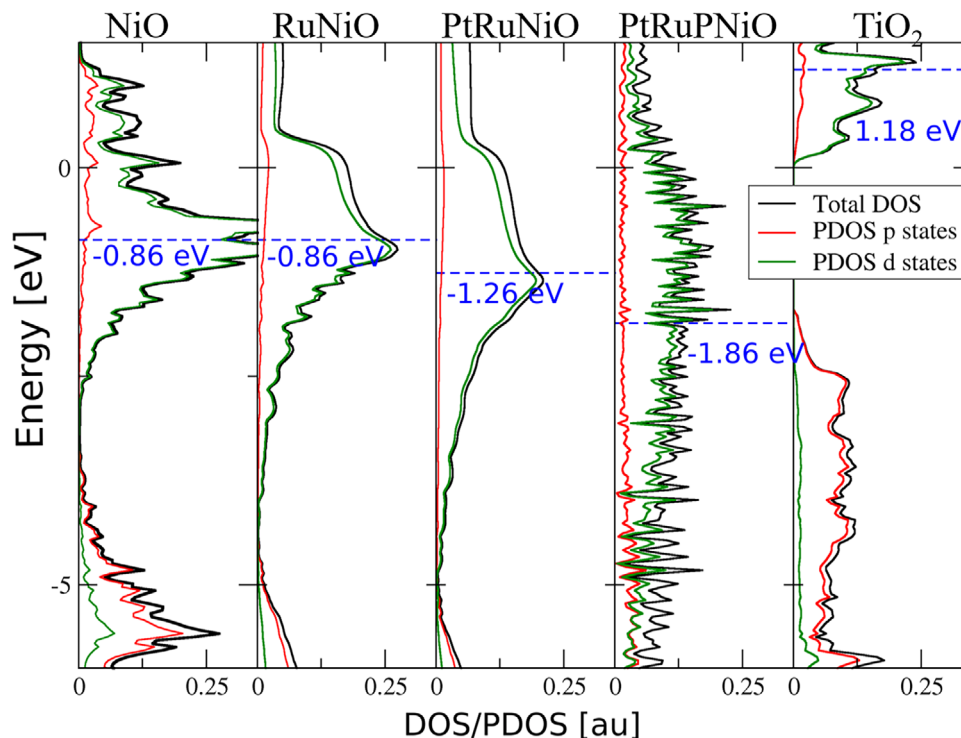
FIGURE 5 Total density of states (DOS) and projected density of states (PDOS) of (from left to right) NiO, RuNiO, PtRuNiO, PtRuPNiO, and TiO$_2$ (rutile). Total DOS (black) and PDOS for $l = 1$ (red, 2sp and 3p) and $l = 2$ (green, 3d, 4d, and 5d) are shown. DOS and PDOS have been normalized to unit. The chemical potential is shown as the energy corresponding to 50% occupancy of d states (blue line). In going from NiO to PtRuPNiO, a broadening of PDOS and extension to lower energies are observed, with an associated lowering of the chemical potential, which favors charge transfer from TiO$_2$ (right n figure). The disordered, high-entropy PtRuPNiO is characterized by localized states that give a spiky appearance to the DOS/PDOS.

states) shows a broadening of states and an associated shift in the chemical potential to lower values (from left to right in Figure 5), favoring charge transfer from TiO$_2$ (more details are provided in Supporting Information). In addition, Figure 4F shows a chronopotentiometric stability analysis for the us-PtRuPNiNiO@TiO$_x$ sample at –10 mA cm^{-2}. It exhibited excellent stability for 16 h, where the first 1.5 h was the activation phase for reaching a fixed potential. X-ray diffraction patterns of PtRuPNiO@TiO$_x$ before and after the stability test showed similar features (Figure 4F). Moreover, the transmission electron microscopy images showed no noticeable changes in the morphology and composition (Figure S12). These results demonstrate the strong interactions between PtRuPNiO and the TiO$_x$ support during the HER and the stabilizing effect of TiO$_x$ on PtRuPNiO against leaching.

2.4 | Entropic contribution to overcoming immiscibility

U-SEO-P induced a high local discharge temperature under ultrasonic irradiation, enabling the synthesis of uniform us-NPs in three systems: us-PtGaNiPNiO@TiO$_x$, us-

PtInNiPNiO@TiO$_x$, and us-PtRuNiPNiO@TiO$_x$ (Figures S13–S15). The high local discharge temperature would effectively increase the entropic contribution ($T\Delta S_{\mathrm{mix}}$) to the Gibbs free energy and overcome the mixing enthalpy (ΔH_{mix}) that may cause phase immiscibility. The ΔH_{mix} values of most atom couples, including Pt–Ga, Pt–Ni, Pt–In, Pt–Ru, Ga–Ni, and Ni–In, were negative, especially in more concentrated systems (mole fraction of A ≈ mole fraction of B), which implies that the systems were miscible (Figure 6A,D,G,K). On the other hand, the Ni–Ru system showed positive ΔH_{mix} values, which caused a large positive ΔH_{mix} field in the Pt–Ru–Ni ternary system (Figure 6G,K). Moreover, the ΔH_{mix} values of the Pt–Ru–Ni system deviated less from 0 than those of the Pt–Ga–Ni and Pt–In–Ni systems.

ΔS_{mix} also depended on the system components (Figure 6B,E,H,K). For the Pt–Ga–Ni and Pt–In–Ni systems, ΔS_{mix} became higher as Ga or In was depleted. On the other hand, the Pt–Ru–Ni system with equimolar composition had the highest ΔS_{mix} compared with the Pt–Ga–Ni and Pt–In–Ni systems. The ΔG_{mix} values at 2000 and 3000 K were calculated using the equation: $\Delta G_{\mathrm{mix}} = \Delta H_{\mathrm{mix}} - T\Delta S_{\mathrm{mix}}$. The trend in ΔG_{mix} was similar to that in ΔH_{mix} because the latter was much lower than
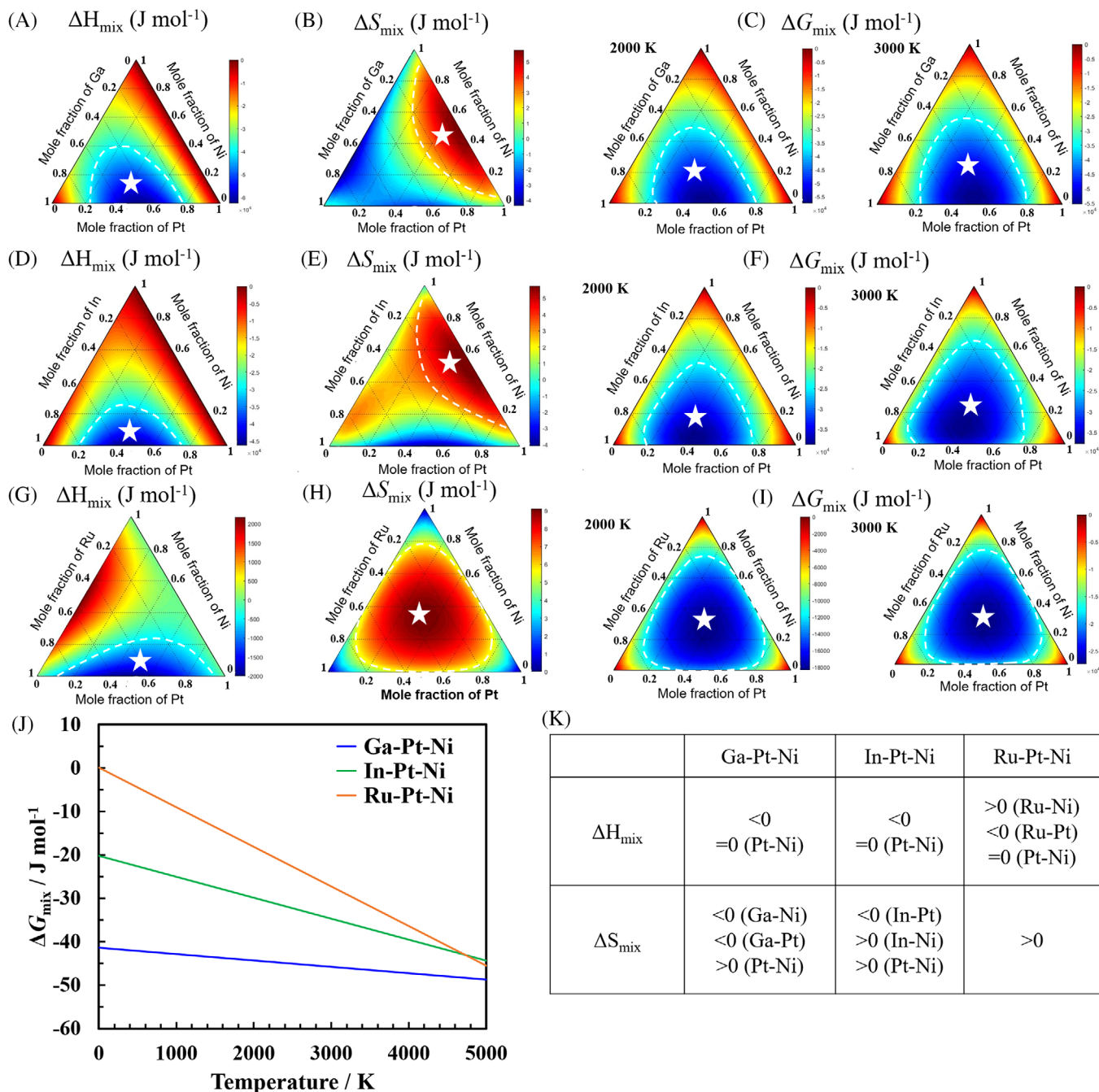
FIGURE 6 Thermodynamic data for the solid–solution formation of us-PtGaNiPNiO@TiO$_x$, us-PtInNiPNiO@TiO$_x$, and us-PtRuNiPNiO@TiO$_x$. (A, D, and G) Mixing enthalpies (ΔH_{mix}), (B, E, and H) mixing entropies (ΔS_{mix}), and (C, F, and I) Gibbs free energies (ΔG_{mix}) of the (A–C) Pt–Ga–Ni, (D–F) Pt–In–Ni, and (G–I) Pt–Ru–Ni systems. (J) ΔG_{mix} as a function of the temperature at equimolar compositions. (K) Signs of ΔH_{mix} and ΔS_{mix} in different ternary systems.

$T\Delta S_{mix}$ (Figure 5C,F,I). However, the trends in ΔG_{mix} and ΔS_{mix} were similar for the Pt–Ru–Ni system because of the (i) low $|\Delta H_{mix}|$, (ii) high ΔS_{mix} throughout the whole composition range, and (iii) high local discharge temperature. As presented in Figure 5J, the Pt–Ru–Ni system exhibited the largest decrease in ΔG_{mix} with temperature owing to the high ΔS_{mix}. The parameter pair, $T\Delta S_{mix}$ and ΔH_{mix}, can be used to effectively optimize

the chemical composition of us-NPs because a high $T\Delta S_{mix}$ and low ΔH_{mix} theoretically lead to high chemical stability. Considering only either ΔS_{mix} or ΔH_{mix} does not guarantee phase miscibility. A low ΔH_{mix} endows us-NPs with high stability in an alloy.[36–39] The high ΔS_{mix} of the Pt–Ru–Ni system enhanced not only the miscibility to form the us-PtRuNiPNiO@TiO$_x$ catalyst but also the HER performance. Compared with us-PtGaNiPNiO@TiO$_x$ and

us-PtInNiPNiO@TiO$_x$, us-PtRuNiPNiO@TiO$_x$ exhibited an enhanced electrocatalytic HER activity (Figure 4). The HER activity increased upon increasing the miscibility to 0.39 mF cm^{-2} and decreased in the absence of Ru primarily owing to the cocktail effect and diffusion hysteresis effect of the high-entropy alloy (HEA).

In addition to the optimum $T\Delta S_{mix}$ and ΔH_{mix} values, the synthesis method involving high local electron temperatures and ultrasonic irradiation promoted uniform alloy formation, rapid thermal decomposition, and reduction of the metal salt precursors to metals. Moreover, this method encouraged in-depth diffusion, alleviated lattice distortion to stabilize the structures of us-HEA against elemental aggregation and nanoscale phase separation, and ensured a single solid–solution structure.

In conclusion, the large decrease in ΔG_{mix} with temperature enabled by the multicomponent system guarantees that lattice strain can be easily overcome by a very high temperature ($\sim$2000 K) using both plasma discharge and ultrasonic irradiation. In addition, these processes provide vibrations that upset the system, which would increase ΔH_{mix} owing to the ΔS_{mix} contribution (Figure 6I,J). This would cause the us-HEA system to become entirely miscible and induce the formation of uniform NPs on TiO$_x$. Our strategy paves the way for preparing nanomaterials and alloys with tunable compositions that have a wide range of applications. Therefore, an optimized temperature in the range of 1500–4000 K is essential for mixing all the metallic elements in one NP and preventing agglomeration, resulting in a uniform us-HEA on TiO$_x$.[39–45]

3 | CONCLUSIONS

We established a scalable synthesis approach (LV-PE) for fabricating us-NP systems comprising different strongly immiscible metals. This approach uses rich Pt cores generated during the first liquid–liquid phase reaction under ultrasonic irradiation and low-voltage plasma. This treatment imitates thermal diffusion, allowing the arrangement of inaccessible metal combinations. Furthermore, control experiments were performed to verify the significant effect of the treatment on the uniform formation of us-NPs. All prepared us-NP systems showed a single-phase solid–solution alloy structure without phase separation, in which the metals, even in strongly repelling combinations, were exceptionally mixed. Different metals with varying lattice strains and atomic radii were uniformly distributed throughout a single NP. Benefiting from the expanded tuning range of the active sites, the synthesized us-NPs exhibited excellent HER activity and durability (over 20 cycles) during the reduction reaction. Our study further expands the spectrum of dissimilar metals and allows for a range of strongly immiscible metal combinations in different metal oxides, including NiO, Al$_2$O$_3$, In$_2$O$_3$, and MgO.

4 | METHODS

4.1 | Synthesis of the PtRuNiNiO@TiO$_2$ catalyst

A porous TiO$_2$ support was deposited on a Ti alloy (20 mm × 30 mm × 2 mm), which was used as an anode. This anode was connected to a stainless steel plate, which was used as the counter electrode, and immersed in an aqueous solution consisting of 5 g L^{-1} KOH, 30 g L^{-1} C$_2$H$_6$O$_2$, 8 g L^{-1} K$_3$PO$_4$, 0.5 L water, and 1.5 L ethanol (pH $\sim$12) in a 2-L glass vessel equipped with a magnetic stirrer. Subsequently, a frequency of 50 Hz and ultrasonic irradiation at 28, 40, and 138 W were applied to the submerged anode for 60 s to stabilize the electrolyte temperature at approximately 273 K by water cooling. Simultaneously, 20 mL of metal precursors (0.5 g L^{-1}; Pt(NO$_3$)$_2$, Ru(NO$_3$)$_3$, and NiO as NPs) were added dropwise ($\sim$1 drop s^{-1}) to a phosphate-based electrolyte. In this process, a porous TiO$_2$ support and PtRuNiNiO NPs were created concurrently owing to the reducing agent (C$_2$H$_6$O$_2$), high temperature, and pressure generated from the discharge channel. Finally, the prepared catalyst was rinsed three times with ethanol and dried under vacuum.

4.2 | Synthesis of the PtGaNiNiO@TiO$_2$ and PtInNiNiO@TiO$_2$ catalysts

The LV-PE procedure for preparing PtGaNiNiO@TiO$_2$ and PtInNiNiO@TiO$_2$ was similar to that for preparing PtRuNiNiO@TiO$_2$. The other LV-PE parameters were the same as those described above.

4.3 | Characterization

HRTEM images were obtained using a scanning transmission electron microscope (FEI, Tecnai F20) at an acceleration voltage of 200 kV. HAADF-STEM images and the corresponding EDS elemental mappings were obtained using the same instrument. The morphology and physicochemical properties of the prepared catalysts were analyzed by scanning electron microscopy (Hitachi, S-4800), XPS (Horiba, XploRA PLUS), PXRD (PANalytical, X'Pert PRO MPD) using Cu Kα radiation, a focused ion beam (Helios, NanoLab 600), Raman spectroscopy (Horiba, XploRA PLUS), and liquid chromatography–mass spectroscopy (Q Exactive Vanquish, Thermo Fisher).

4.4 | Catalytic activity and electrochemical measurements

Details are provided in the Supporting Information.

4.5 | Thermodynamic calculations and computational details

Details are provided in the Supporting Information.

AUTHOR CONTRIBUTIONS

Wail Al Zoubi: Conceptualization; methodology; investigation; formal analysis; writing—original draft; review & editing. **Abdullah Al Mahmud**: Formal analysis and writing—orginal draft. **Farah Hazmatulhaq**: Formal analysis and writing—orginal draft. **Mohammad R. Thalji**: Formal analysis and writing—orginal draft. **Stefano Leoni**: Conceptualization; methodology; investigation; formal analysis; writing—original draft; review & editing. **Jee-Hyun Kang**: Formal analysis and writing—orginal draft. **Young Gun Ko**: Formal analysis and writing—orginal draft.

CONFLICT OF INTEREST STATEMENT
The authors declare no conflict of interest.

ORCID
Wail Al Zoubi https://orcid.org/0000-0003-4213-8481
Mohammad R. Thalji https://orcid.org/0000-0002-0946-6136

REFERENCES

1. Sanker M, Dimitratos N, Miedziak PJ, Wells PP, Keily CJ, Hutchings GJ. Designing bimetallic catalysts for a green and sustainable future. *Chem Soc Rev*. 2012;41(24):8099-8139.
2. Zhang J, Gao Z, Wang S, et al. Origin of synergistic effects in bicomponent cobalt oxide-platinum catalysts for selective hydrogenation reaction. *Nat Commun*. 2019;10(1):4166.
3. Minamihara H, Kusada K, Wu D, et al. Continuous-flow reactor synthesis for homogeneous 1 nm-sized extremely small high-entropy alloy nanoparticles. *J Am Chem Soc*. 2022;144(26):11525-11529.
4. Behrens M, Zander S, Kurr P, et al. Performance improvement of nanocatalysts by promoter induced defects in the support material: methanol synthesis over Cu/ZnO:Al. *J Am Chem Soc*. 2013;135(16):6061-6068.
5. Briggs NM, Barret L, Wegener EC, et al. Identification of active sites on supported metal catalysts with carbon nanotube hydrogen highways. *Nat Commun*. 2018;9(1):3827.
6. Phaahlamohlaka TN, Kumi DO, Dlamini MW, et al. Effects of Co and Ru intimacy in Fischer–Tropsch catalysts using hollow carbon sphere supports: assessment of the hydrogen spillover processes. *ACS Catal*. 2017;7(3):1568-1578.
7. Zhang H, Zhang XG, Jie W, et al. Revealing the role of interfacial properties on catalytic behaviors by in situ surface-enhanced Raman spectroscopy. *J Am Chem Soc*. 2017;139(30):10339-10346.
8. Karim W, Spreafico C, Kleibert A, et al. Catalyst support effects on hydrogen spillover. *Nature*. 2017;541(7635):68-71.
9. Samad JE, Blanchard J, Sayag C, Louis C, Regalbuto JR. The controlled synthesis of metal-acid bifunctional catalysts: the effect of metal: acid ratio and metal-acid proximity in Pt silica-alumina catalysts for nheptane isomerization. *J Catal*. 2016;342:203-212.
10. Cheng K, Gu B, Liu X, Kang J, Zhang Q, Wang Y. Direct and highly selective conversion of synthesis gas into lower olefins: design of a bifunctional catalyst combining methanol synthesis and carbon-carbon coupling. *Angew Chem Int Ed Engl*. 2016;128(15):4803-4806.
11. Al Zoubi W, Allaf AW, Assfour B, Ko YG. Concurrent oxidation –reduction reactions in a single system using a low-plasma phenomenon: excellent catalytic performance and stability in the hydrogenation reaction. *ACS Appl Mater Interfaces*. 2022;14(5):6740-6753.
12. Kamil MP, Al Zoubi W, Yoon DK, Yang HW, Ko YG. Surface modulation of inorganic layer via soft plasma electrolysis for optimizing chemical stability and catalytic activity. *Chem Eng J*. 2020;391:123614.
13. Ge H, Shen Z, Wang Y, et al. Design of high-performance and sustainable Co-free Ni-rich cathodes for next-generation lithium-ion batteries. *SusMat*. 2024;4(1):48-71.
14. Feng G, Ning F, Song J, et al. Sub-2 nm ultrasmall high-entropy alloy nanoparticles for extremely superior electrocatalytic hydrogen evolution. *J Am Chem Soc*. 2021;143(41):17117-17127.
15. Lu X, Mohedano M, Blawert C, et al. Plasma electrolytic oxidation coatings with particle additions—a review. *Surf Coat Technol*. 2016;307:1165-1182.
16. Al Zoubi W, Assfour B, Allaf AW, Leoni S, Kang JH, Ko YG. Experimental and theoretical investigation of high-entropy-alloy/support as a catalyst for reduction reactions. *J Energy Chem*. 2023;81:132-142.
17. Hoseini A, Yarmand B, Kolahi A. Inhibitory effects of hematite nanoparticles on corrosion protection function of TiO_2 coating prepared by plasma electrolytic oxidation. *Surf Coat Tech*. 2021;409:126938.
18. Chu X, Wang Y, Cai L. Boosting the energy density of aqueous MXene-based supercapacitor by integrating 3D conducting polymer hydrogel cathode. *SusMat*. 2022;2(3):379-390.
19. White JL, Bocarsly AB. Enhanced carbon dioxide reduction activity on indium-based nanoparticles. *J Electrochem Soc*. 2016;163(6):H140-H416.
20. Dang D, Zou H, Xiong Z, et al. High-performance, ultralow platinum membrane electrode assembly fabricated by in situ deposition of a Pt shell layer on carbon-supported Pd nanoparticles in the catalyst layer using a facile pulse electrodeposition approach. *ACS Catal*. 2015;5(7):4318-4324.

21. Deng K, Xu Y, Yang D, et al. Pt–Ni–P nanocages with surface porosity as efficient bifunctional electrocatalysts for oxygen reduction and methanol oxidation. *J Mater Chem A*. 2019;7(16):9791-9797.

22. Chu C, Rao S, Ma Z, Han H. Copper and cobalt nanoparticles doped nitrogen-containing carbon frameworks derived from CuO-encapsulated ZIF-67 as high-efficiency catalyst for hydrogenation of 4-nitrophenol. *App Catal B*. 2019;256:117792.

23. Sheng Y, Liu Y, Yin Y, et al. Rh promotional effects on Pt–Rh alloy catalysts for chemoselective hydrogenation of nitrobenzene to p-aminophenol. *Chem Eng J*. 2023;452:139448.

24. Cheong WC, Yang W, Zhang J, et al. Isolated iron single-atomic site-catalyzed chemoselective transfer hydrogenation of nitroarenes to arylamines. *ACS Appl Mater Interfaces*. 2019;11(37):33819-33824.

25. Li Z, Zhang M, Dong X, et al. Strong electronic interaction of indium oxide with palladium single atoms induced by quenching toward enhanced hydrogenation of nitrobenzene. *App Catal B*. 2022;313:121462.

26. Han A, Zhang J, Sun W, et al. Isolating contiguous Pt atoms and forming Pt–Zn intermetallic nanoparticles to regulate selectivity in 4-nitrophenylacetylene hydrogenation. *Nat Commun*. 2019;10(1):3787.

27. Liu Y, Sheng Y, Yin Y, et al. Phosphorus-doped activated coconut shell carbon-anchored highly dispersed Pt for the chemoselective hydrogenation of nitrobenzene to *p*-aminophenol. *ACS Omega*. 2022;7(13):11217-11225.

28. Zhao Y, Kumar PV, Tan X, et al. Modulating Pt–O–Pt atomic clusters with isolated cobalt atoms for enhanced hydrogen evolution catalysis. *Nat Commun*. 2022;13(1):2430.

29. Abbas SA, Kim SH, Iqbal MI, Muhammad S, Yoon W-S, Jung K-D. Synergistic effect of nano-Pt and Ni spine for HER in alkaline solution: hydrogen spillover from nano-Pt to Ni spine. *Sci Rep*. 2018;8(1):213969.

30. Zhang J, Qu X, Han Y, et al. Engineering PtRu bimetallic nanoparticles with adjustable alloying degree for methanol electrooxidation: enhanced catalytic performance. *Appl Catal B: Environ*. 2020;263:118345.

31. Al Zoubi W, Putri RAK, Abukhadra MR, Ko YG. Recent experimental and theoretical advances in the design and science of high-entropy alloy nanoparticles. *Nano Energy*. 2023;110:108362.

32. Du H, Kong RM, Guo X, Qu F, Li J. Recent progress in transition metal phosphides with enhanced electrocatalysis for hydrogen evolution. *Nanoscale*. 2018;10(46):21617-21624.

33. Kandel MR, Pan UN, Paudel DR, Dhakal PP, Kim NH, Lee JH. Hybridized bimetallic phosphides of Ni–Mo, Co–Mo, and Co–Ni in a single ultrathin-3D-nanosheets for efficient HER and OER in alkaline media. *Composites Part B*. 2022;239:109992.

34. Yu L, Zhang J, Dang Y, et al. In situ growth of Ni$_2$P–Cu$_3$P bimetallic phosphide with bicontinuous structure on self-supported NiCuC substrate as an efficient hydrogen evolution reaction electrocatalyst. *ACS Catal*. 2019;9(8):6919-6928.

35. McCrory CCL, Jung S, Peters JC, Jaramillo TF. Benchmarking heterogeneous electro catalysts for the oxygen evolution reaction. *J Am Chem Soc*. 2013;135(45):16977-16987.

36. Wang Y, Luo W, Luo L, Li Y, Zhao Y, Li Z. Synthesis of high-entropy-alloy nanoparticles by a step-alloying strategy as a superior multifunctional electrocatalyst. *Adv Mater*. 2023;35(36):2302499.

37. Kwon IS, Lee SJ, Kim JY, et al. Composition-tuned (MoWV)Se$_2$ ternary alloy nanosheets as excellent hydrogen evolution reaction electrocatalysts. *ACS Nano*. 2023;17(3):2968-2979.

38. Ye YF, Wang Q, Lu J, Liu CT, Yang Y. High-entropy alloys: challenges and prospects. *Mater Today*. 2016;19(6):349-362.

39. Dippo OF, Vecchio KS. A universal configurational entropy metric for high-entropy materials. *Scr Mater*. 2021;201:113974.

40. Al Zoubi W, Nashrah N, Putri RAK, Allaf AW, Ko YG. Strong dual-metal–support interactions induced by low-temperature plasma phenomenon. *Mater Today Nano*. 2022;18:100213.

41. Shokry R, Aman D, Abd El Salam HM, et al. Linker regulation of CoO@Cu/C derived from self-assembly of MOF to enhance catalytic activity of organic contaminants. *Mater Today Nano*. 2024;25:100444.

42. Su BJ, Foo JJ, Ling GZS, Ong WJ. Synergistic redox toward co-production of H$_2$O$_2$ and value-added chemicals: dual-functional photocatalysis to achieving sustainability. *SusMat*. 2024;e192.

43. Zhang X, Li F, Yang S, et al. Multi-scale structure engineering of covalent organic framework for electrochemical charge storage. *SusMat*. 2024;4(1):4-33.

44. Shao C, Zhao Y, Qu L. Recent advances in highly integrated energy conversion and storage system. *SusMat*. 2022;2(2):142-160.

45. Zhang Y, Zheng W, Wu H, et al. Tungsten oxide-anchored Ru clusters with electron-rich and anti-corrosive microenvironments for efficient and robust seawater splitting. *SusMat*. 2024;4(1):106-115.

SUPPORTING INFORMATION

Additional supporting information can be found online in the Supporting Information section at the end of this article.